Prediction of Two-Point Statistics on Cones in High-Speed Flow via Instability Wave Theory

Jianhui Cheng* and Steven A. E. Miller[†]
University of Florida, Gainesville, Florida, 32611, USA

Instability waves create intense aerodynamic loading that is spatially coherent near the leading edges of flight-vehicles. This loading creates intense vibrations within the underlying structures. Previous investigations have shown that the nose bluntness alters the stability and transition process. The objective of the present paper is to further study the effects of nose bluntness on the pressure fluctuations on the vehicle surface via linear stability theory. This paper presents the results of a free-stream Mach 3.50 axisymmetric flow over a seven degree half-angle cone with varying nose radii. Ten cones with nose radii ranging from 0.038 to 38.1 mm ($r_1 \sim r_{10}$), covering both the small and large bluntness regions, are used to study the effects of nose bluntness on stability, spectra of fluctuating pressure, and spatial coherence. It is found that small nose radii do not alter these properties. The larger nose radii show lower growth rates due to the thick boundary layer and lower pressure fluctuation spectrum. However, variations of the growth of the Mack-mode instability do not demonstrate similarity with small nose radii when the nose radii is larger than $r_7 = 3.969$ mm. The pressure spectrum decreases as the nose radii increases except for small nose radii. The value of spatial coherence decreases with increasing frequency.

Nomenclature

Symbols	Description		Greek Symbols	
A, B, C	Matrices		α	Streamwise wavenumber
C	Sutherland's constant		β	Spanwise wavenumber
c_P	Specific heat		Γ	Spatial coherence
f	Frequency		γ	Ratio of specific heats
h_1, h_2, h_3	Scale factors		κ	Body curvature
i	Imaginary number		λ	Second coefficient of viscosity
k	Thermal conductivity		μ	First coefficient of viscosity
L	Length of the cone along axis		ν	Kinematic viscosity
l	Length scale		Φ	Viscous dissipation
m_{12}, m_{23}, m_{13}	Curvature coefficient		$\boldsymbol{\phi}$	Disturbance vector
n	Azimuthal mode		ϕ	Single-point wavenumber spectrum
p	Pressure		Ψ_{PP}	Pressure cross-power spectra density matrix
r	Local radius		ψ	Wave angle
R	Gas constant		ω	Radial frequency
R_{PP}	Spatial-time correlation function		ρ	Density
T	Temperature		τ	Time lag
t	Time		θ	Half angle of cone
$\boldsymbol{u}$	Velocity vector		ξ	Separation distance vector
u_P	Phase speed			

Superscripts and subscripts			Non-Dimensional Numbers	
*	Dimensional value		M_e	Edge Mach number
e	Edge value		σ	Prandtl number
n	Normal direction		Re	Reynolds number
∞	Ambient or infinity			

I. Introduction

Lᴇᴀᴅɪɴɢ edge geometries of flight-vehicles experience intense aerodynamic loading at high-speeds. Instability waves that lead to transition to turbulence create large pressure fluctuations on the surface of vehicles. The action of the

*Ph.D. Candidate, Department of Mechanical and Aerospace Engineering, University of Florida, 231 MAE-A, P.O.Box 116250, chengjianhui@ufl.edu, AIAA Student member.

[†]Assistant Professor, Department of Mechanical and Aerospace Engineering, University of Florida, 231 MAE-A, P. O. Box 116250, saem@ufl.edu / saemiller@gmail.com, AIAA Senior / Lifetime member.

stochastic pressure distribution associated with instability waves and turbulence provides the driving force that excites the underlying structure [1, 2]. This excitation in turn generates intense vibrations on the payload, personnel, or other critical flight-vehicle systems [3, 4] during rocket ascent [1]. Reduction of these vibrations will increase flight-vehicle safety [5], reduce vibration induced failure of satellites [5], and reduce noise for astronauts [5, 6]. Therefore, accurate external wall-pressure predictions are necessary for leading edge geometries at supersonic and hypersonic speeds. This will provide designers a tool to make improved predictions that may result in lower weight of vehicles and reduce harmful vibrations.

Previous Approaches

A turbulent boundary layer (TBL) is characterized by the development of large-scale structures from instabilities and turbulent eddies ranging through the entire cascade. High-speed boundary layers are unstable and instability waves form. The wall pressure fluctuations induced by instability waves and turbulent flow are broadband in nature. Thus, the wall pressure statistics are difficult to calculate, predict, or measure [6] as they are an imprint of instability waves or turbulence at the wall. The fluctuating pressures at the wall are usually described via statistics as the turbulent flow is random in nature. A large number of empirical and theoretical models [7–10] have been developed to describe these random wall-pressure fluctuations, and the parameters of these models are fitted with experimental measurement. One of the models for power spectral density (PSD) of the TBL wall pressure fluctuations was introduced by Corcos [9]. Corcos [9] developed a statistical empirical model that fit a large number of measurements of the pressure field from an attached flow, and provided the cross-power spectral density (CSD) of the wall pressure fluctuations. The Corcos [9] model is well suited to describe the statistics of wall-pressure fluctuations induced by high-speed subsonic flows. Palumbo [11] has also applied the Corcos [9] model and others to higher-speed supersonic flows using test data, where it was shown that wind-tunnel calibration often did not match flight-test data. Graham [12] summed, outlined and compared different types of empirical models. These empirical models and corresponding experiments demonstrate a need for more first-principle based prediction approaches, as often the empirical models must be re-calibrated for particular flight-vehicles.

Both instability waves and large-scale turbulent structures have been studied both analytically and experimentally. The existence of large-scale coherent motions within high-speed flows has been identified [13, 14] and defined via statistical means [15], instantaneous flow patterns [16], stability theory [17], and techniques from dynamical systems theory [18]. There are different stable and unstable modes with corresponding effects within boundary layer flows. One important unstable wave is called the first mode (Mack's first mode), which is an extension of the Tollmien-Schlichting (TS) instability waves present in incompressible flows [19]. This wave is most amplified when it is an oblique wave at supersonic Mach numbers and represents viscous instability at low Mach numbers [19]. Additionally, there exist an infinite number of modes when the wave speed is supersonic within boundary layer flows (Mode I, Mode II, etc. [20]), and the second mode (Mack's second mode) forms. The second mode is significant at boundary layer edge Mach numbers (M_e) approximately above 4, has growth rates much higher than the first mode, and is most amplified when the wave angle is zero or two-dimensional wave. In fact, studies also showed that the Mack modes (the first and the second modes) are slightly unstable in multiple regions of varying frequencies [13, 20]. The first modes are slightly unstable in the range of lower frequencies (i.e. $f^* \leq 112$ kHz for $M_\infty = 7.99$). The conventional second mode are unstable at higher frequencies [20]. The first mode is responsible for transition when the wall is adiabatic for freestream Mach number (M_∞) up to approximately 7 [21].

Stability theory has been applied to study the transition of the boundary layer and the effect of heat exchange on the vehicle surface (see for example Malik and Spall [19], Malik [22], Knisely and Zhong [23], Laible et al. [24]). It has been shown that the first and second mode instability waves play important roles in the transition process [13, 25]. Various parameters, including body configurations, the Mach number, wall temperature, entropy layer, and roughness, would affect the stability and transition within boundary layer flows [13]. The effects of nose bluntness [25–30] on transition are investigated both experimentally and numerically. In experimental measurements of cones with nose radii ranging from 0.7937 to 38.1 mm were tested and transition locations (x_T) were measured [26]. Flight test data of transition position at different conditions are summarized [27]. However, there are discrepancies between experimental measurement and numerical predictions. In general, the results of numerical predictions are larger than the corresponding experimental measurements. For example, x_T is larger than 3.2 m (maximum cone length for numerical simulation) from numerical calculations, whereas x_T is 0.24 m from experimental measurement for $M_\infty = 5.46$ with nose radius 38.1 mm [26].

Present Approach

The objective of our research is to study the effects of instability waves within high-speed boundary layer flows via computing the pressure fluctuations from the instability waves on cones with different leading edge radii. These geometries are similar to the leading edges of supersonic and hypersonic flight-vehicles. They represent prototypical geometry for investigating boundary layer stability and transition [31]. We seek to study the effects of two-point statistics and loading from instability waves during rocket launching. Two-point statistics are used for rocket and flight-vehicle structural vibration estimates, and some analysts use a simpler approach involving single values of intensity and length-scale. Here, we explore a combination of traditional approaches to find two-point statistics over cones at high-speed flow and how they can be altered with different nose radii.

In this paper, we apply the linear stability theory (LST) within boundary layer flows described by Malik [22] and Malik and Spall [19] to obtain the instability wave solutions and construct the pressure fluctuations on the cone surface. The time-averaged velocity field, pressure, and temperature distribution over a cone are computed via numerical simulation and validated by comparing with publicly available data in the literature (see Laible et al. [24] and Gross and Fasel [31]). The base flow-field (time-averaged Navier-Stokes equations) is used as an argument for the instability equations. These instability solutions include local wavenumbers and shape functions at varying azimuthal modes and frequencies at multiple streamwise locations. The LST predictions are validated with publicly available results of Mayer [32]. Additionally, the stability properties, single-point wall pressure spectrum, and spatial coherence of cones with varying nose radii are computed and analyzed. These methods and results facilitate our understanding of the effects of large-scale structures as the driving force within high-speed boundary layers. This will allow us to develop a database of flow-fields that can be used to understand the changes of coherence and intensity from instability waves as a function of cone configuration.

In the next section, the LST is presented along with our approach for calculating the pressure fluctuations from instability waves. In the results section, the mean flow-field of a base case are computed and validated firstly. The value of different nose radii are listed and the mean flow-field of each case are computed. The stability results of base case are validated first. The stability properties of each case are computed and compared. The single-point wall pressure spectrum and spatial coherence from instability waves are shown and analyzed. Finally, we summarize the present effort and propose the future work.

II. Methodology

Linear Stability Theory

We use LST to predict the unstable modes within the boundary layer that develops within supersonic flows. We assume that the flow is governed by the compressible Navier-Stokes equations, energy equation, and ideal gas law. The ideal gas law is used for simplicity in our accompaning CFD simulations and for the subsequent analysis. These equations and overall method are discussed in Malik and Spall [19]. The equations governing the flow of a viscous compressible ideal gas include the continuity equation

$$\frac{\partial \rho}{\partial t} + \nabla \cdot (\rho \boldsymbol{u}) = 0, \tag{1}$$

the momentum equation

$$\rho \left[\frac{\partial \boldsymbol{u}}{\partial t} + (\boldsymbol{u} \cdot \nabla)\boldsymbol{u} \right] = -\nabla p + \nabla \cdot [\lambda (\nabla \cdot \boldsymbol{u})I] + \nabla \cdot [\mu(\nabla u + \nabla u^{tr})], \tag{2}$$

the energy equation

$$\rho c_P \left[\frac{\partial T}{\partial t} + (\boldsymbol{u} \cdot \nabla)T \right] = \nabla \cdot (k \nabla T) + \frac{\partial p}{\partial t} + (\boldsymbol{u} \cdot \nabla)p + \Phi, \tag{3}$$

and the ideal gas law

$$p = \rho RT. \tag{4}$$

Here, c_P is the specific heat, k is the thermal conductivity, p is the pressure, R is the gas constant, T is the temperature, $\boldsymbol{u} = (u, v, w)$ is the velocity vector, μ is the first coefficient of viscosity, $\Phi = \lambda(\nabla \cdot \boldsymbol{u}) + \mu[\nabla \boldsymbol{u} + \nabla \boldsymbol{u}^{tr}]^2/2$ is the viscous

dissipation, λ is the second coefficient of viscosity, and ρ is the density. The perturbation equations that govern the instability waves are derived from the linearized Eqs. (2) to (4) in non-dimensional form. All lengths are scaled by viscous length $l = (v_e^* x^*/u_e^*)^{1/2}$. Here, v_e^* is the dimensional viscosity at the boundary layer edge, where the definition of boundary layer edge values depends on the specific flow conditions. Velocities are scaled by u_e^*, density by ρ_e^*, pressure by $\rho_e^* u_e^{*2}$, time by l/u_e^*, and other variables by their corresponding values at the boundary layer edge position. The instantaneous values of the field variables and parameters in Eqs. (2) to (4) can be expressed as the sum of a mean and a fluctuation quantity

$$
\begin{aligned}
u &= \bar{U} + \tilde{u}, \quad v = \bar{V} + \tilde{v}, \qquad w = \bar{W} + \tilde{w}, \\
p &= \bar{P} + \tilde{p}, \quad T = \bar{T} + \tilde{T}, \qquad \rho = \bar{\rho} + \tilde{\rho}, \\
\mu &= \bar{\mu} + \tilde{\mu}, \quad \lambda = \bar{\lambda} + \tilde{\lambda}, \qquad k = \bar{k} + \tilde{k},
\end{aligned}
\tag{5}
$$

where $\bar{\{\cdot\}}$ denotes the non-dimensional mean quantity and $\tilde{\{\cdot\}}$ denotes the non-dimensional fluctuating quantity.

In this study, we consider the flow over a cone, which is an axisymmetric body at zero incidence. The body-fitted orthogonal curvilinear coordinates x, y, and z are used, where x is the streamwise coordinate along the cone surface, y is the coordinate normal to the surface, and z is the azimuthal direction. The scale factors are determined via coordinate transformations and are defined as

$$
h_1 = 1 + \kappa(x)y; \quad h_2 = 1; \quad h_3 = r + y\cos(\theta),
\tag{6}
$$

where $\kappa = -\frac{d\theta}{dx}$ is local body curvature, θ is the half-angle of the cone, and r is the local body radius.

The curvature coefficients are

$$
m_{13} = \frac{1}{h_1}\frac{\partial h_1}{\partial y}; \quad m_{21} = \frac{1}{h_1 h_2}\frac{\partial h_2}{\partial x}; \quad m_{23} = \frac{1}{h_2}\frac{\partial h_2}{\partial y}.
\tag{7}
$$

Here, $m_{13} = 0$ is the streamwise curvature for cone cases, m_{21} is related to body divergence due to increase in the body radius, and m_{23} represents transverse curvature effect.

For cone geometries, m_{21} and m_{23} are

$$
m_{21} = \frac{d(\ln r)/dx}{1 + \epsilon y} = \frac{l\sin\theta}{r(1 + \epsilon y)}
\tag{8}
$$

and

$$
m_{23} = \frac{\epsilon}{1 + \epsilon y},
\tag{9}
$$

where $\epsilon = l\cos(\theta)/r$.

We assume that the flow is locally parallel within the boundary layer on the cone surface to simplify the LST prediction. This is a common assumption for LST analysis. Specifically, we assume that the gradients of the mean flow in the streamwise direction and the mean vertical velocity are negligible. However, the numerical prediction of the mean flow-field does not make this assumption. Under these assumptions we set

$$
\bar{U} = \bar{U}(y); \quad \bar{V} = 0; \quad \bar{T} = \bar{T}(y); \quad \bar{P} = \bar{P}(y); \quad \bar{\rho} = \bar{\rho}(y),
\tag{10}
$$

and

$$
\bar{W}(y) = 0,
\tag{11}
$$

because of the axisymmetric nature of the time-averaged flow.

We also make a number of other minor simplifying assumptions. Firstly, due to the boundary layer assumption, pressure ($\bar{p}$) is constant across the layer and is equal to $1/(\gamma M_e^2)$, where $M_e = u_e^*/\sqrt{\gamma R T_e^*}$. The viscosity $\bar{\mu}$ is calculated using Sutherland's law. Sutherland's law is

$$
\bar{\mu} = \bar{T}^{\frac{3}{2}}\frac{1 + C/T_\infty^*}{\bar{T} + C/T_\infty^*},
\tag{12}
$$

4

where $C = 110.4$ K is a constant or effective temperature and T_∞^* represents the dimensional free-stream temperature. Moreover, $\tilde{\mu}$, $\tilde{\lambda}$, and $\tilde{k}$ are related to temperature as

$$\tilde{\mu} = \frac{d\bar{\mu}}{d\bar{T}}\tilde{T}, \quad \tilde{\lambda} = \frac{d\bar{\lambda}}{d\bar{T}}\tilde{T}, \quad \text{and} \quad \tilde{k} = \frac{d\bar{k}}{d\bar{T}}\tilde{T}. \tag{13}$$

The disturbance amplitudes are assumed to be small enough so that they do not interact in a nonlinear fashion to avoid nonlinear effects. We assume that the solution of the instability waves can be expressed in the following form

$$\tilde{\boldsymbol{\phi}}(x, y, z, t) = \hat{\boldsymbol{\phi}}(y) \exp[i(\alpha x + \beta z - \omega t)], \tag{14}$$

which consists of a spatially varying function and an exponentially varying spatial periodic function. Here, $\tilde{\boldsymbol{\phi}}$ is a five-element vector defined by $\{\tilde{u}, \tilde{v}, \tilde{p}, \tilde{T}, \tilde{w}\}$, $\hat{\boldsymbol{\phi}}(y)$ is the shape function of each element vector, α and $\beta = nl/r$ (n is the azimuthal mode number) are the wavenumbers in the streamwise and spanwise directions, $\omega = 2\pi f^* l/u_e^*$ is non-dimensional frequency, and f^* is dimensional frequency. In general, α, β, and ω are complex numbers. In this paper, we focus on spatial stability and set ω and β as real numbers.

After using these assumptions and dropping the bar notation for mean flow variables, the compressible linear instability equations for boundary layer flow over a cone are

$$\frac{d^2\hat{u}}{dy^2} + (c_1 T' + m_{23})\frac{d\hat{u}}{dy} + i\alpha_0 l_1 \frac{d\hat{v}}{dy} + c_1 U' \frac{d\hat{T}}{dy}$$
$$+ \left[ic_3 R_e/(\mu T) - l_2 \alpha_0^2 - \beta_0^2 + i\alpha_0 l_2 m_{21} - l_2 m_{21}^2\right]\hat{u} + \left[i\alpha_0(c_1 T' + l_1 m_{23}) - R_e U'/(\mu T) - l_2 m_{21}^2\right]\hat{v} - (i\alpha_0 R_e/\mu)\hat{p}$$
$$+ [c_1(U'' + m_{23}U' + i\alpha_0 l_0 U m_{21} - l_2 U m_{21}^2) + c_2 U'T']\hat{T} - [\alpha_0\beta_0 l_1 + i\beta_0 l_3 m_{21}]\hat{w} = 0, \tag{15}$$

$$\frac{d^2\hat{v}}{dy^2} + \frac{(i\alpha_0 + m_{21})l_1}{l_2}\frac{d\hat{u}}{dy} + (c_1 T' + m_{23})\frac{d\hat{v}}{dy} - \frac{R_e}{l_2\mu}\frac{d\hat{p}}{dy} + \frac{c_1 U m_{21} l_0}{l_2}\frac{d\hat{T}}{dy}$$
$$+ \frac{i\beta_0 l_1}{l_2}\frac{d\hat{w}}{dy} + \left[c_1 T'(i\alpha_0 + m_{21})l_0/l_2 - m_{21}m_{23}\right]\hat{u} + \left[\{ic_3 R_e/\mu T - \beta_0^2 + i\alpha_0 m_{21} + c_1 T' m_{23} l_0\}/l_2 - m_{23}^2\right]\hat{v}$$
$$+ \left[\{i\alpha_0 c_1 U' + c_1(U' m_{21} l_1 - U m_{21} m_{23}) + c_2 U T' m_{21} l_0\}/l_2 - c_1 U m_{21} m_{23}\right]\hat{T} + [i\beta_0(c_1 T' l_0 - m_{23} l_3)/l_2]\hat{w} = 0, \tag{16}$$

$$\frac{d\hat{v}}{dy} + (i\alpha_0 + m_{21})\hat{u} + [m_{23} - T'/T]\hat{v} + \gamma M_e^2(m_{21}U - ic_3)\hat{p} - \left[\frac{m_{21}U - ic_3}{T}\right]\hat{T} + i\beta_0\hat{w} = 0, \tag{17}$$

$$\frac{d^2\hat{T}}{dy^2} + c_4 U'\frac{d\hat{u}}{dy} + c_4 U m_{21} l_0 \frac{d\hat{v}}{dy} + (2k'/k + m_{23})\frac{d\hat{T}}{dy}$$
$$+ c_4[i\alpha_0 U m_{21} l_0 + U m_{21}^2 l_2]\hat{u} + [c_4\{i\alpha_0 U' + U m_{21} m_{23} l_0\} - \sigma R_e T'/(\mu T)]\hat{v} - [ic_3 c_4 R_e/(2\mu)]\hat{p}$$
$$+ \left[ic_3 R_e \sigma/(\mu T) - \beta_0^2 + i\alpha_0 m_{21} + c_1 c_4\{0.5(U'^2 + U^2 m_{21}^2 l_2)\} + m_{23}k'/k + k''/k\right]\hat{T} + i\beta_0 c_4 U m_{21} l_2 \hat{w} = 0. \tag{18}$$

and

$$\frac{d^2\hat{w}}{dy^2} + i\beta_0 l_1 \frac{d\hat{v}}{dy} + (c_1 T' + m_{23})\frac{d\hat{w}}{dy} + (i\beta_0 m_{21} l_3 - \alpha_0\beta_0 l_1)\hat{u} + i\beta_0(c_1 T' + l_3 m_{23})\hat{v} - \frac{i\beta_0 R_e}{\mu}\hat{p}$$
$$+ i\beta_0 c_1 U m_{21} l_2 \hat{T} + \left[(ic_3 - m_{21}U)R_e/(\mu T) - l_2\beta_0^2 + i\alpha_0 m_{21} - m_{21}^2 - m_{23}(c_1 T' + m_{23})\right]\hat{w} = 0, \tag{19}$$

where $()' \equiv d/dy$, $l_q = q + \lambda/\mu$, $\alpha_0 = \alpha/h_1$, $\beta_0 = \beta/h_2$, $R_e = \rho_e u_e l/\mu_e$ is Reynolds number, $\sigma = \mu c_p/k = 0.7$ is Prandtl number for this computation and

$$c_1 = \frac{1}{\mu}\frac{d\mu}{dT}, \quad c_2 = \frac{1}{\mu}\frac{d^2\mu}{dT^2}, \quad c_3 = -(\alpha U - \omega), \quad c_4 = 2(\gamma - 1)M_e^2\sigma. \tag{20}$$

5

The linear stability equations can be written as a system of equations as

$$\left(A\frac{d^2}{dy^2} + B\frac{d}{dy} + C\right)\hat{\boldsymbol{\phi}} = 0,$$ (21)

where A is a diagonal matrix and B and C are 5×5 matrices.

The boundary conditions at the wall are

$$y = 0; \quad \hat{\boldsymbol{\phi}}_1 = \hat{\boldsymbol{\phi}}_2 = \hat{\boldsymbol{\phi}}_4 = \hat{\boldsymbol{\phi}}_5 = 0,$$ (22)

and the boundary conditions in the far-field are

$$y \to \infty; \quad \hat{\boldsymbol{\phi}}_1, \hat{\boldsymbol{\phi}}_2, \hat{\boldsymbol{\phi}}_4, \hat{\boldsymbol{\phi}}_5 \to 0.$$ (23)

We seek to ascertain the instability wave solution represented by $\hat{\boldsymbol{\phi}}$. First, we calculate the local wavenumber by solving the eigenvalue problem defined by Eqs. (21) through (23). The phase speed and growth rate of the instability wave are obtained from the complex wave number, $\alpha = \alpha_r + i\alpha_i$. The real part of the complex wave number, α_r, represents the number of axial oscillations per unit length (axial wave number). The phase speed is obtained from $u_p = \omega\alpha_r^{-1}$. The phase speed, u_p, is a measure of the convection speed of the instability wave. The growth rate is given by the negative part of the complex wavenumber, $-\alpha_i$. If the growth rate is positive, then the instability wave is amplified, whereas, the instability wave becomes damped if the growth rate is negative.

There are two main methods to solve the discretized system. The first is the local method, and the second is the global method [19]. The global method yields all the eigenvalues of the discretized system. Both methods require that the equations be discretized by the finite difference [19, 22] or spectral approach [19]. The problem is then reduced to a linear algebraic system. Four different schemes and detailed analyses were introduced to discretize the system of equations [19]. In this study, the global method via finite difference is adapted. The mean velocity and density within the equations are found from numerical simulation using a CFD solver.

Cross-Power Spectral Density of Pressure from Instability Waves

We can directly predict the wall pressure field from the instability waves based on the solution of Eq. (21) at multiple axial positions on the cone surface. We choose the most amplified instability waves in the azimuthal direction as the source of the driving force [33]. Equation (14) represents the form of a single instability wave. However, in high Reynolds number high-speed flow, there is a wide spectrum of instability waves [34]. As a linear theory is adapted, we superimpose solutions to obtain contributions from multiple waves. The pressure fluctuations field from instability waves can be constructed via integration over ω as

$$\tilde{p}(\boldsymbol{x}, t) = \int_{-\infty}^{\infty} \hat{p}(y) \exp\left[i(\alpha x + \beta z - \omega t)\right] d\omega.$$ (24)

Here, the instability wave solution with angular frequency $-\omega$ and azimuthal wavenumber $-\beta$ is related to the solution with positive frequency ω and wavenumber β (see [34, 35]). For example, the relation for pressure ($\hat{p}$) is $\hat{p}(\boldsymbol{x}, -\omega, -\beta) = \hat{p}^*(\boldsymbol{x}, \omega, \beta)$, where the asterisk denotes the complex conjugate. We do not focus on the overall amplitudes of the predicted instability waves. Scaling the solution results in another solution.

The spatial coherence of pressure fluctuations from instability waves is calculated via

$$\Gamma_{pp}(\boldsymbol{\xi}, \omega) = \frac{1}{2\pi}\int_{-\infty}^{\infty}\langle\tilde{p}(\boldsymbol{x}, t)\tilde{p}(\boldsymbol{x} + \boldsymbol{\xi}, t + \tau)\rangle\exp(-i\omega\tau)d\tau = \frac{1}{2\pi}\int_{-\infty}^{\infty}R_{pp}(\boldsymbol{\xi}, \tau)\exp(-i\omega\tau)d\tau,$$ (25)

where $R_{pp}(\boldsymbol{\xi}, \tau)$ is the space-time cross-correlation function, $\boldsymbol{\xi}$ is the spatial separation vector, and τ is the time lag.

Furthermore, in a typical vibration-acoustic problem of TBL flows, the semi-empirical models, such as the Corcos model [9] and modified Corcos model [1], have been proposed to express the excitation from pressure fluctuations within TBL flows. Such models can be modeled in terms of a point pressure spectrum term multiplied by a spatial expression [6] as

$$\Psi_{pp}(\boldsymbol{\xi}, \omega) = \phi(\omega)\Gamma_{pp}(\boldsymbol{\xi}, \omega),$$ (26)

where $\phi(\omega)$ is the single-point wall pressure fluctuation spectrum.

6

III. Results and Analysis

In this section, we compute and validate the mean flow-field of a cone configuration with a circular nose of constant radius. The growth rate, phase-speed, and eigenfunctions of the test case are also computed and validated. The single-point wall pressure spectrum and spatial coherence of pressure fluctuations from instability waves on the cone surface for different nose radii are presented.

The Steady Mean Flow-Field Validation and Computation

The Stanford University Unstructured (SU2) open source software suite (see Palacios et al. [36] for details) is used to compute the time-averaged flow-field. The SU2 solver is finite-volume based, and we solve the steady compressible NS equations in axisymmetric form. We computed the $M_\infty = 3.50$ flow of Gross and Fasel [31] as the test case. In this test case, the cone half angle is (θ) 7°, the nose radii is 0.038 mm, and the length of the cone (L) is 0.3556 m. The other freestream parameters used for the simulations are freestream temperature and density are 90.1 K and 8.74×10^{-2} kg/m^3, respectively. Figure 1(a) shows the entire flow region (0.3556 m $\times$ 0.2 m). A structured grid is used with an exponential distribution. This allows for decreased grid spacing near the wall. This grid point distribution around the nose region is shown in Fig. 1(b). We set the first mesh cell off the wall as 1×10^{-6} m, which is estimated for a desired Y+ value less than 1 using flat-plate compressible boundary layer theory. Additionally, the grid independence study is applied. On the cone surface, the no-penetration and the no-slip conditions are enforced. The wall is set to be adiabatic ($\partial T / \partial y_n = 0$).
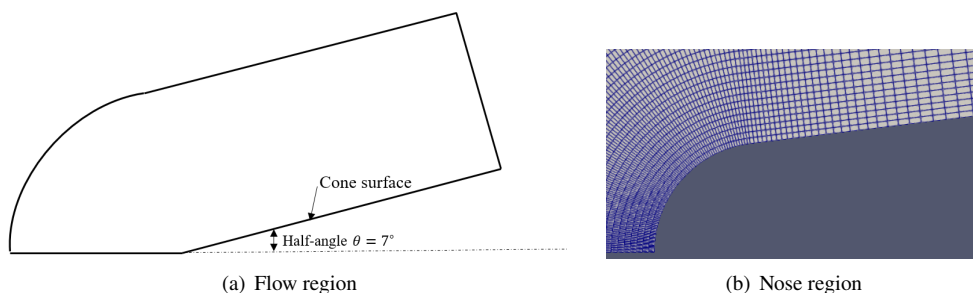

(a) Flow region   (b) Nose region

Fig. 1   The domain and computational grid near the nose.

Two grid sizes are used to examine grid independence. The coarse grid size is 201 points in the wall normal direction and 201 points in the streamwise direction, and the fine grid uses 401 points in the wall normal direction and 201 points in the streamwise direction. Figure 2 shows the residual and Y+ of the coarse grid simulation. These graphs show that the numerical simulation converges, and the grid distribution is sufficient to resolve the flow-field.
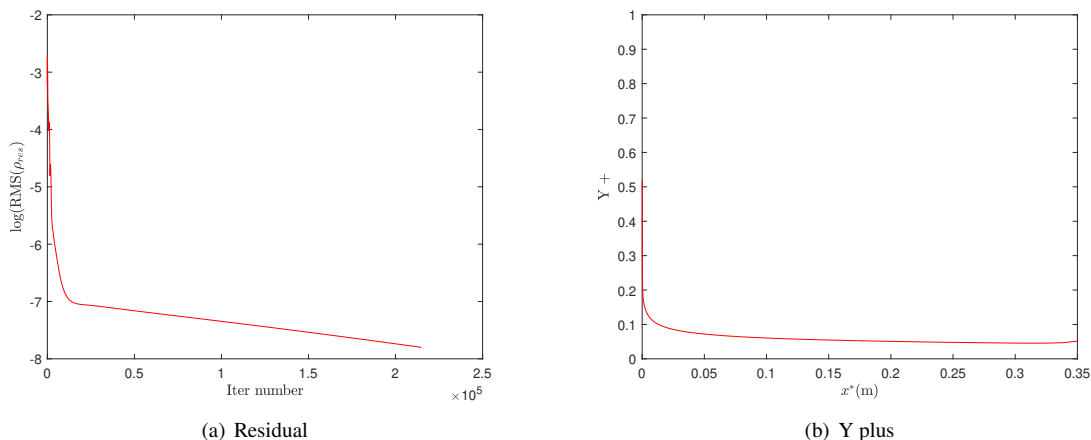

(a) Residual   (b) Y plus

Fig. 2   Residual and Y plus of numerical simulation with coarse grid distribution.

Comparisons of flow-field between two mean profiles from numerical simulation and Gross and Fasel [31] (shown as

"Ref") are made with axial velocity and temperature distributions at three streamwise locations corresponding to Gross and Fasel [31] of x^*/L = 0.624, 0.76, and 0.825 are shown in Fig. 3. In the Fig. 3, the axial velocity and temperature are normalized with the boundary layer edge values, which are directly extracted from the CFD solution. The positions of the boundary layer edge of Laible [37] are defined as the point where the wall normal derivative, $\partial U/\partial y$, of the velocity component parallel to the cone surface (U) is minimum. In this paper, we choose the positions as the value of derivative less than a small value (0.05). We apply the infinity norm of the relative error to quantify the error among the profiles in the Fig. 3. The error of flow-field profiles of the coarse and fine grid is 1.4% at x^*/L =0.76 based on the variation of T in the cross-stream direction, which shows grid independence of the current numerical simulations. In addition, the maximum infinity norm of relative error between the numerical simulation and Gross and Fasel [31] (shown as "Ref") is 0.8% at x^*/L =0.624. Therefore, the coarse grid distribution is used in the following analysis.

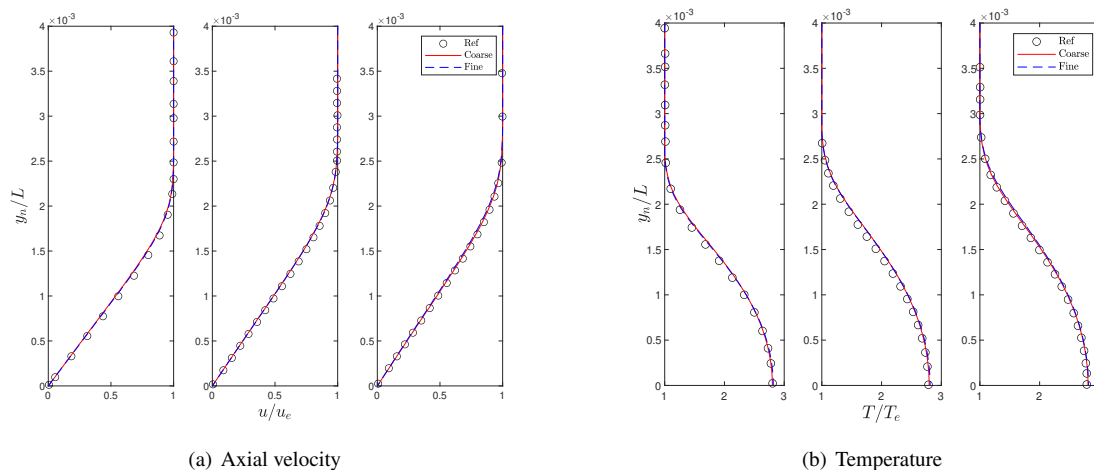(a) Axial velocity

(b) Temperature

Fig. 3   The comparison of axial velocity and temperature at different streamwise positions.

In this paper, cones with ten different nose radii with the same freestream conditions as the test case are studied because the nose bluntness is an important factor for stability and transition properties for boundary layer flows. We choose the nose radii based on the validation case up to 38.1 mm and indicate the ten nose radii as r_1 to r_{10}, respectively. The specific value of each case is shown within Table 1.

Table 1   Nose radii (mm).

r_1	r_2	r_3	r_4	r_5	r_6	r_7	r_8	r_9	r_{10}
0.038	0.076	0.152	0.38	1.14	1.905	3.969	7.938	15.876	38.1

For the flow region, we extend the test case region to 3.5 m × 3.5 m, which is a large value to guarantee a region is large enough for future analysis (i.e. changing free-stream Mach numbers or determining heating source location). The grid size is 267 points in the wall normal direction and 301 points in the streamwise direction. Numerical predictions are conducted in serial on the local high-performance computing cluster at University of Florida.

Figure 4 shows the Mach number contours for cones with nose radii r_1, r_7, and r_{10} of part of the entire flow region (0.3 m × 0.2 m). As the nose radii increases, the shock detached from the leading edge, or bow shock appears. In addition, an entropy layer appears in the region near the leading nose for the larger nose radii cases (r_7 and r_{10}). In the downstream direction, the entropy layer gradually merges with the boundary layer.

Stability Validation and Computation

In this section, the linear stability results of the test case are validated firstly. The stability parameters of our LST solver and results from Mayer [32] are shown in Table 2. The values of β and ω are given for the oblique wave and spatial stability computation. The eigenvalue, $\alpha = \alpha_r + i\alpha_i$, is found from the previously described eigenvalue solver. The oblique wave angle (ψ) is computed via $\tan^{-1}(\beta/\alpha_r)$. Several factors are important for the calculation of
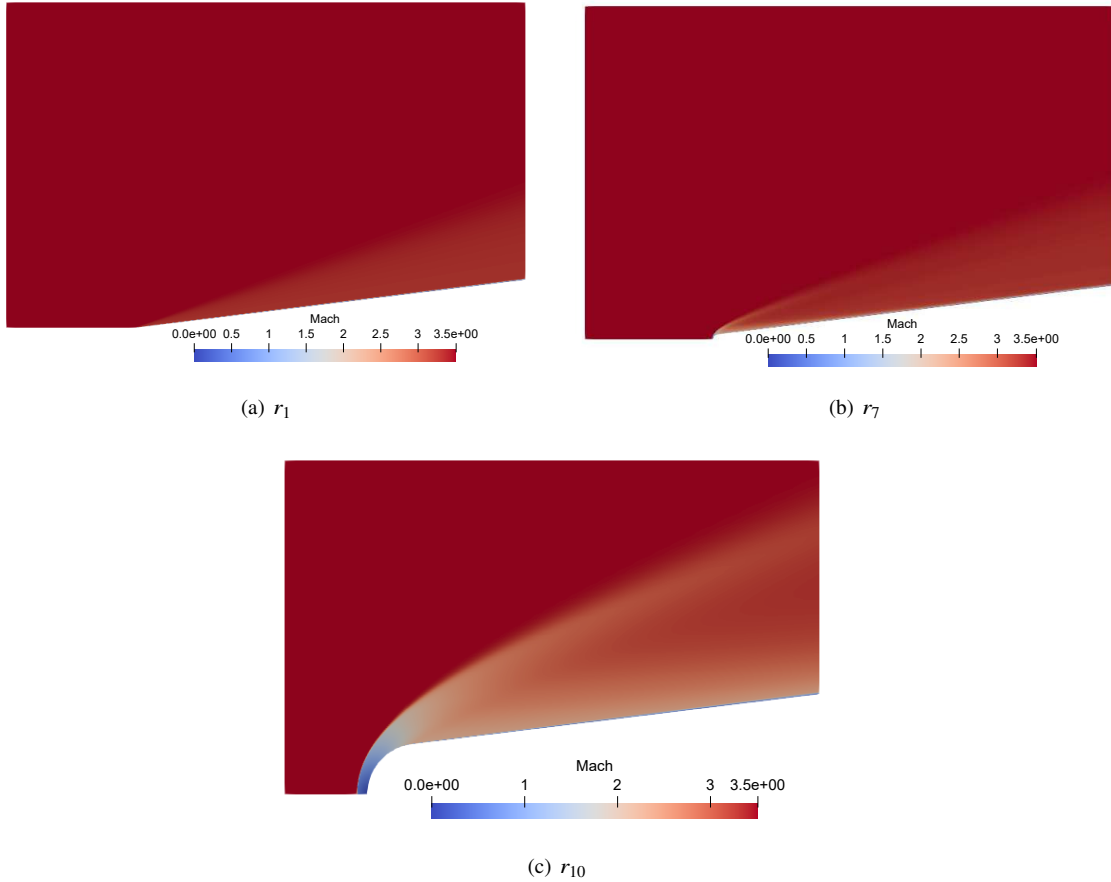
8

(a) r_1

(b) r_7

(c) r_{10}

Fig. 4   Mach number contours of r_1, r_7, and r_{10} conditions.

eigenvalues, which include the number of grid points, the discretization method, and the flow-field. We note there are some discrepancies between our calculation and the reference solution [32] due to these factors.

Table 2   Stability Parameters.

	f^*	n	α	ψ	u_p
Mayer [32]	23.415 kHz	21	350.1-22.5 i	N/A	N/A
LST	23.415 kHz	21	353.2-14.96 i	65.93°	0.64

Figure 5 shows the comparison of the amplitude of eigenfunctions in the wall-normal direction between the LST and the predictions of Mayer [32], where the distance in the normal direction is normalized by the boundary layer thickness, δ. Here, "Ref" indicates the results from Mayer [32]. It can be seen that similar variations of the eigenfunctions exist between our LST solver and Mayer [32]. There are discrepancies between LST and Mayer [32] results near the wall region for the u-velocity component and temperature eigenfunctions. The positions of the maximum value of $\hat{u}$ are at y_n/δ=0.6154 and 0.5654 for LST and Mayer [32]. The error is 8.9% for the $\hat{u}$ component. The error of $\hat{T}$ is approximately 7.2%. The results of our LST prediction and that of Mayer [32] are in good agreement at the higher y_n value.

We focus on prediction of the unsteady coherent forcing on the vehicle surface due to instability waves from the Mack mode within the present work. These are dominant at low supersonic speeds. We restrict the frequency to be less than 75 kHz for the flow conditions and the azimuthal modes less than 40. Figure 6 shows the maximum growth rates for all frequencies and azimuthal modes of leading edge radii r_1 to r_{10} along the streamwise direction. It can be seen that the maximum growth rates are very similar for r_1 to r_4. This similarity indicates small leading edge radii for cones
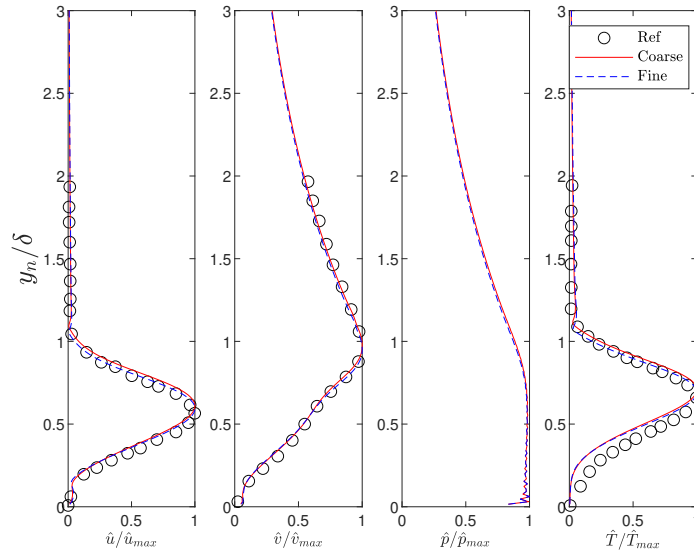
Fig. 5 Comparison of amplitudes of eigenfunctions between the LST prediction and Mayer [32] (Ref).

do not alter maximum growth rate. For larger leading edge radii, r_4 to r_7, the growth rates decrease as the nose radius increase monotonically. There are no apparent trends for r_7 to r_{10}, especially in the region close to the leading edge. This is potentially caused by the entropy layer that forms for larger leading edge radii. For r_1 to r_6 conditions, there is an obvious peak of growth rates, then growth rates decrease. However, the peak locations of growth rates for r_7 to r_{10} are not clear. The peak locations of each case are 0.14, 0.14, 0.14, 0.18, 0.23, 0.31, 0.46, 0.30, 0.26, and 0.55 m, respectively. The locations of maximum growth rates move to downstream directions as the nose radii increases (r_4 to r_7).
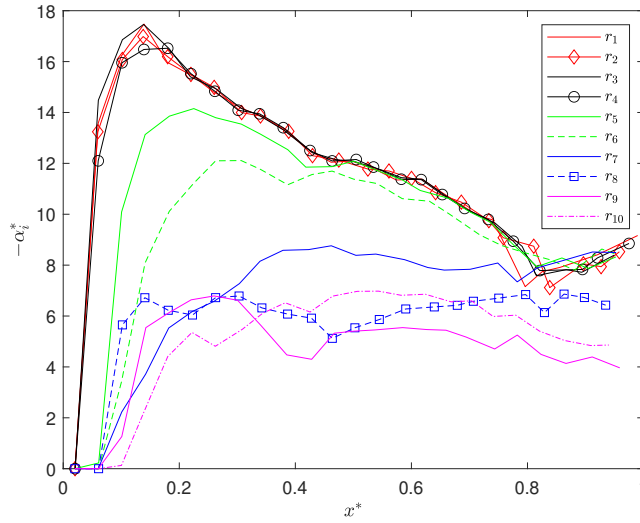

Fig. 6 Comparison of maximum growth rate for all frequencies and azimuthal modes along streamwise direction for r_1 to r_{10}.

Single-point Wall Pressure Spectrum

Figure 7 shows the comparisons of single-point wall pressure spectrum over frequency ranges at x^*=0.14, x^*=0.31, x^*=0.46, and x^*=0.62 m for r_1 to r_{10}. The spectrum value increase firstly and then decrease. It can be seen that the maximum spectrum value of each case in the upstream direction is lower than that of downstream direction. The corresponding frequency of maximum spectral value decreases with increasing streamwise location. For r_1 and r_4, the spectral values are close at the selected locations because the small nose radii do not alter maximum growth rate. The spectrum value of r_5 and r_6 are closer to r_1 to r_4 except at $x^* = 0.14$ m because the growth rates of r_5 and r_6 show large difference relative to r_1 to r_4. For r_7 to r_{10}, the spectrum value is lower than that of r_1 to r_6 when ω^* is larger than the frequency corresponding to the maximum spectrum value.

(a) $x^* = 0.14$(m)

(b) $x^* = 0.31$(m)

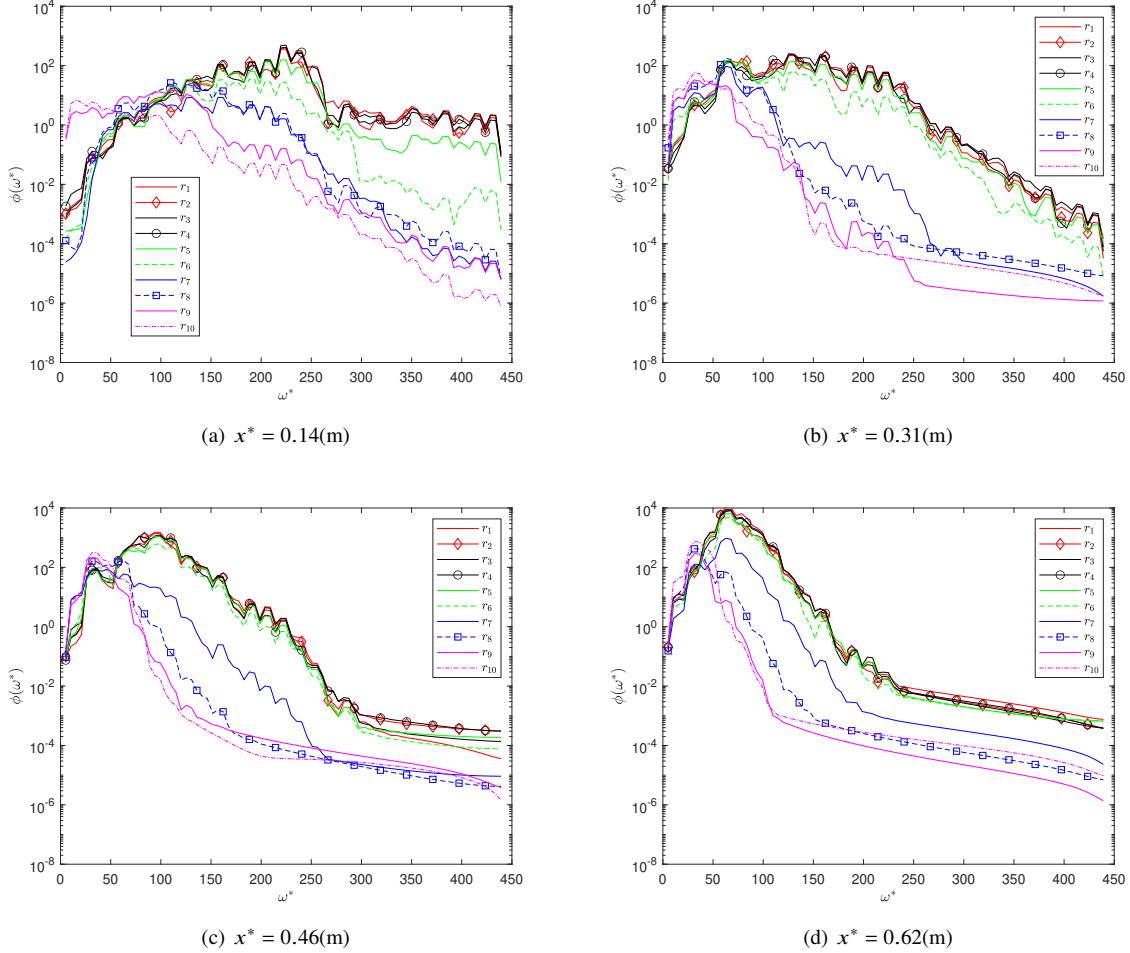(c) $x^* = 0.46$(m)

(d) $x^* = 0.62$(m)

Fig. 7   Comparison of single-point wall pressure spectrum over frequency range at x^*= 0.14, 0.31, 0.46, and 0.62 m for r_1 to r_{10} conditions.

Spatial Coherence

Figure 8 shows the spatial coherence for nose radii from r_1 through r_{10}, where the reference point is the peak position of each case of Fig. 6. The results show the spatial coherence variations on the separation distance and dimensional frequency. It can be seen that the spatial coherence shows similar trends for r_1 through r_4 (Fig. 8(a) through 8(d)), which is consistent with the growth rate distribution for these four cases. Figures 8(a) to 8(e) (r_1 to r_5) show higher value of spatial coherence when $\omega^* \geq 50$ kHz, and the separation distance between the reference point for higher spatial coherence become smaller as the frequency increases. However, the value of spatial coherence are higher when

ω^* is less than 150 kHz for Fig. 8(g) to 8(i) (r_7 to r_9). We assume that amplified instability waves will show higher spatial coherence than damped instability waves. The growth rates mainly depend on the non-dimensional frequency ($\omega = 2\pi f^* (v_e^* x^* / u_e^*)^{1/2} / u_e^*$), and the instability waves are amplified when ω is within a range, i.e. $0.02 \sim 0.06$. The non-dimensional frequency is related to the dimensional frequency and streamwise locations/length scale. In specific, for the nose radii r_1 through r_4, the reference points (x^*) are smaller so that the instability waves are amplified at higher dimensional frequencies. The value of spatial coherence are higher when 30 kHz$\leq \omega^* \leq$ 350 kHz for r_5 (Fig. 8(e)) and 20 kHz$\leq \omega^* \leq$ 250 kHz for r_6 (Fig. 8(f)) conditions because the length scale increases as the nose radii increase. For r_7 through r_9 conditions (Fig. 8(g) to 8(i)), the positive growth rates of instability waves are at lower dimensional frequency. This is due to a thicker boundary layer and entropy layer caused by larger nose radii. However, Fig. 8(j) (r_{10}) shows higher spatial coherence within the separation distance -0.1 to 0.2 m over all frequencies unexpectedly.
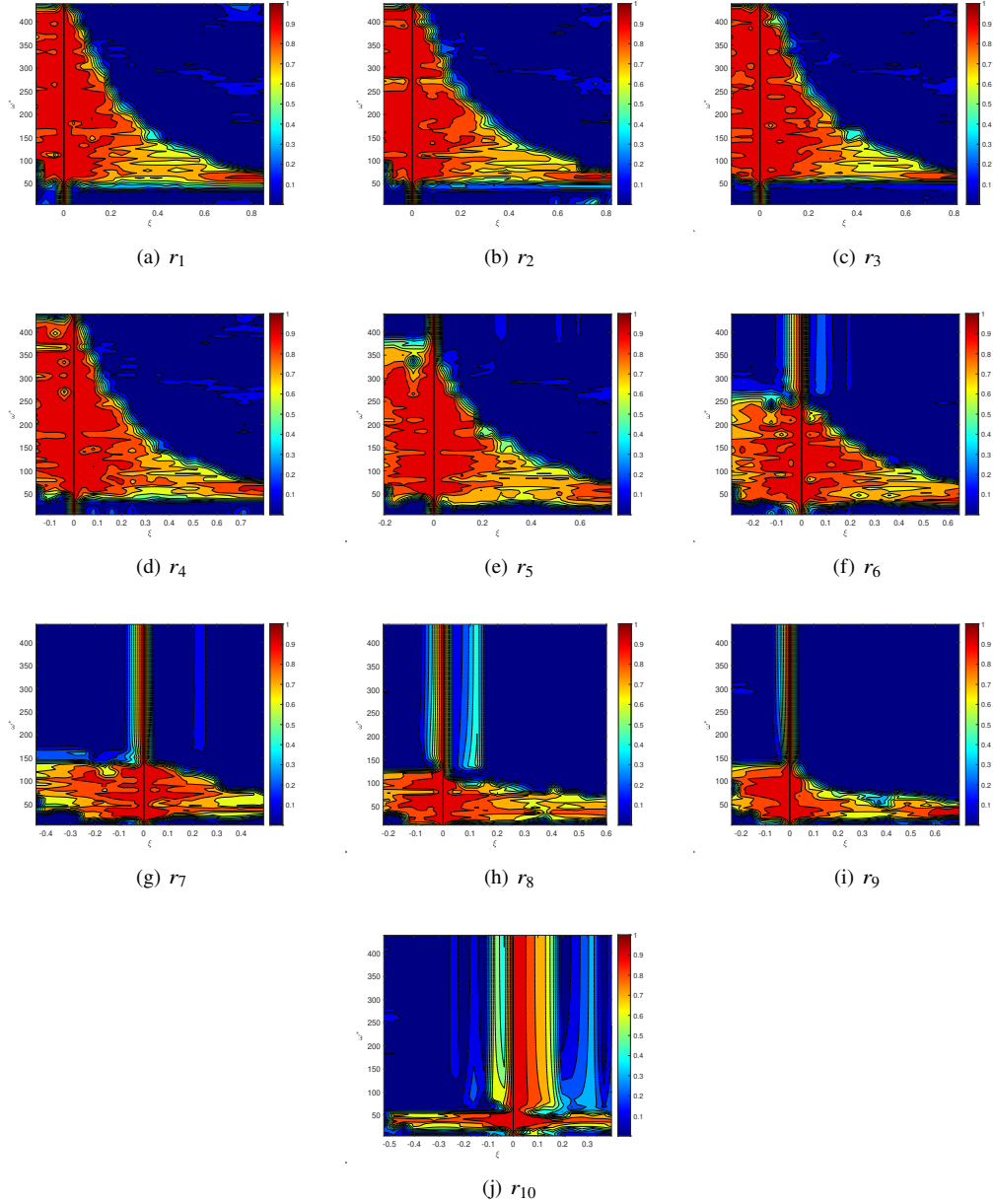

(a) r_1

(b) r_2

(c) r_3

(d) r_4

(e) r_5

(f) r_6

(g) r_7

(h) r_8

(i) r_9

(j) r_{10}

Fig. 8 Spatial coherence of different nose radii from r_1 to r_{10}, where the reference point of each case is at the maximum grow rate along streamwise direction.

IV. Summary and Conclusion

We predict the spectra and spatial coherence due to the pressure induced by instability waves over cones of various radii. The mean-flow variables for instability wave solutions are computed via SU2 and show good agreement with previous investigations. The growth rate and shape functions of instability waves are also validated. The maximum growth rates for frequencies and azimuthal mode numbers of different nose radii along the streamwise direction show that the small leading edge radii for cones do not alter maximum growth rate. Larger leading edge radii have smaller pressure spectral value at higher frequencies. The higher spatial coherence within a small frequency range for larger leading edge radii.

The results of this paper demonstrate the effects of leading edge radii on the growth rate distributions, pressure perturbation spectrum, and spatial coherence, which is beneficial to understand the characters of the driving force causing the vibration during rocket ascent. For $r_1 \sim r_5$ conditions, the higher spatial coherence value is at medium and high frequencies, $\omega^* > 50$ kHz, as the nose radii increase ($r_7 \sim r_9$), the high value of spatial coherence are at relative low frequency $\omega^* < 150$ kHz. The separation distances relative to the reference point become smaller as the frequency increases. Additionally, the approach can be used to choose an appropriate nose radii in the design process by combing the structural analysis to predict vibration. In the future, we plan to alter the flow-field via plasma actuation. The effects of plasma actuators model on the stability properties, pressure spectrum, and spatial coherence will be investigated.

References

[1] Caiazzo, A., D'Amico, R., and Desmet, W., "Use of a Generalized Corcos Model to Predict Flow-Induced Noise in a Cavity-plate System," Proceedings of the 27th International Conference on Noise and Vibration Engineering, ISMA2016 & USD2016, 2016, pp. 1319–1332.

[2] Lubert, C. P., "Sixty Years of Launch Vehicle Acoustics," Proceedings of the Meetings of the Acoustical Society of America 31, 2017. doi:10.1121/2.0000704.

[3] Marchetto, C., Maxit, L., Robin, O., and Berry, A., "Experimental Prediction of the Vibration Response of Panels under a Turbulent Boundary Layer Excitation from Sensitivity Functions," *The Journal of the Acoustical Society of America*, Vol. 143, No. 5, 2018, pp. 2954–2964. doi:10.1121/1.5037362.

[4] Fahy, F. J., "Statistical Energy Analysis: a Critical Overview," *Philosophical Transactions of the Royal Society of London. Series A: Physical and Engineering Sciences*, Vol. 346, No. 1681, 1994, pp. 431–447. doi:10.1098/rsta.1994.0027.

[5] Langenecker, B., "Effect of Sonic and Ultrasonic Radiation on Safety Factors of Rockets and Missiles," *AIAA Journal*, Vol. 1, No. 1, 1963, pp. 80–83. doi:10.2514/3.1474.

[6] da Rocha, J., "Coupled Structural-Acoustic Analytical Models for the Prediction of Turbulent Boundary-Layer-Induced Noise in Aircraft Cabins," Ph.D. thesis, University of Victoria, 2010.

[7] Chase, D., "Modeling the Wavevector-Frequency Spectrum of Turbulent Boundary Layer Wall Pressure," *Journal of Sound and Vibration*, Vol. 70, No. 1, 1980, pp. 29–67. doi:10.1016/0022-460x(80)90553-2.

[8] Ffowcs-Williams, J. E., "Boundary-Layer Pressures and the Corcos Model: a Development to Incorporate Low-Wavenumber Constraints," *Journal of Fluid Mechanics*, Vol. 125, No. -1, 1982, p. 9. doi:10.1017/s0022112082003218.

[9] Corcos, G. M., "The Structure of the Turbulent Pressure Field in Boundary-Layer Flows," *Journal of Fluid Mechanics*, Vol. 18, No. 03, 1964, pp. 353–378. doi:10.1017/s002211206400026x.

[10] Efimtsov, B., "Characteristics of the Field of Turbulent Wall Pressure-Fluctuations at Large Reynolds-Numbers," *Soviet Physics Acoustics-USSR*, Vol. 28, No. 4, 1982, pp. 289–292.

[11] Palumbo, D., "Determining Correlation and Coherence Lengths in Turbulent Boundary Layer Flight Data," *Journal of Sound and Vibration*, Vol. 331, No. 16, 2012, pp. 3721–3737.

[12] Graham, W., "A Comparison of Models for the Wavenumber Frequency Spectrum of Turbulent Boundary Layer Pressures," *Journal of Sound and Vibration*, Vol. 206, No. 4, 1997, pp. 541–565. doi:10.1006/jsvi.1997.1114.

[13] Lee, C., and Jiang, X., "Flow Structures in Transitional and Turbulent Boundary Layers," *Physics of Fluids*, Vol. 31, No. 11, 2019, p. 111301. doi:10.1063/1.5121810.

[14] Robinson, S. K., "Coherent Motions in the Turbulent Boundary Layer," *Annual Review of Fluid Mechanics*, Vol. 23, No. 1, 1991, pp. 601–639. doi:10.1146/annurev.fl.23.010191.003125.

[15] Marusic, I., "On the Role of Large-Scale Structures in Wall Turbulence," *Physics of Fluids*, Vol. 13, No. 3, 2001, pp. 735–743. doi:10.1063/1.1343480.

[16] Morrison, G., and McLaughlin, D., "Noise Generation by Instabilities in Low Reynolds Number Supersonic Jets," *Journal of Sound and Vibration*, Vol. 65, No. 2, 1979, pp. 177–191. doi:10.1016/0022-460x(79)90512-1.

[17] Tam, C. K. W., and Hu, F. Q., "On the Three Families of Instability Waves of High-speed Jets," *Journal of Fluid Mechanics*, Vol. 201, No. 1, 1989, p. 447. doi:10.1017/s002211208900100x.

[18] Delville, J., Ukeiley, L., Cordier, L., Bonnet, J. P., and Glauser, M., "Examination of Large-Scale Structures in a Turbulent Plane Mixing Layer. Part 1. Proper Orthogonal Decomposition," *Journal of Fluid Mechanics*, Vol. 391, 1999, pp. 91–122. doi:10.1017/s0022112099005200.

[19] Malik, M. R., and Spall, R. E., "On the Stability of Compressible Flow Past Axisymmetric Bodies," *Journal of Fluid Mechanics Digital Archive*, Vol. 228, 1991, pp. 443–463. doi:10.1017/s002211209100277x.

[20] Zhong, X., and Ma, Y., "Boundary-layer Receptivity of Mach 7.99 Flow over a Blunt Cone to Free-Stream Acoustic Waves," *Journal of Fluid Mechanics*, Vol. 556, 2006, p. 55. doi:10.1017/s0022112006009293.

[21] Malik, M. R., "Prediction and Control of Transition in Supersonic and Hypersonic Boundary Layers," *AIAA Journal*, Vol. 27, No. 11, 1989, pp. 1487–1493. doi:10.2514/3.10292.

[22] Malik, M., "Numerical Methods for Hypersonic Boundary Layer Stability," *Journal of Computational Physics*, Vol. 86, No. 2, 1990, pp. 376–413. doi:10.1016/0021-9991(90)90106-b.

[23] Knisely, C. P., and Zhong, X., "Sound Radiation by Supersonic Unstable Modes in Hypersonic Blunt Cone Boundary Layers. I. Linear Stability Theory," *Physics of Fluids*, Vol. 31, No. 2, 2019, p. 024103. doi:10.1063/1.5055761.

[24] Laible, A., Mayer, C., and Fasel, H., "Numerical Investigation of Supersonic Transition for a Circular Cone at Mach 3.5," *38th Fluid Dynamics Conference and Exhibit*, AIAA Paper No. 2008-4397, 2008. doi:10.2514/6.2008-4397.

[25] Esfahanian, V., "Computation and Stability Analysis of Laminar Flow over a Blunt Cone in Hypersonic Flow," Ph.D. thesis, Ohio State University, 1991.

[26] Lei, J., and Zhong, X., "Linear Stability Analysis of Nose Bluntness Effects on Hypersonic Boundary Layer Transition," *Journal of Spacecraft and Rockets*, Vol. 49, No. 1, 2012, pp. 24–37. doi:10.2514/1.52616.

[27] Schneider, S. P., "Flight Data for Boundary-Layer Transition at Hypersonic and Supersonic Speeds," *Journal of Spacecraft and Rockets*, Vol. 36, No. 1, 1999, pp. 8–20. doi:10.2514/2.3428.

[28] Rosenboom, I., Hein, S., and Dallmann, U., "Influence of Nose Bluntness on Boundary-Layer Instabilities in Hypersonic Cone Flows," *30th Fluid Dynamics Conference*, American Institute of Aeronautics and Astronautics, 1999. doi:10.2514/6.1999-3591.

[29] Kufner, E., Dallmann, U., and Stilla, J., "Instability of Hypersonic Flow Past Blunt Cones - Effects of Mean Flow Variations," *23rd Fluid Dynamics, Plasmadynamics, and Lasers Conference*, American Institute of Aeronautics and Astronautics, 1993. doi:10.2514/6.1993-2983.

[30] Balakumar, P., and Malik, M. R., "Discrete Modes and Continuous Spectra in Supersonic Boundary Layers," *Journal of Fluid Mechanics*, Vol. 239, No. -1, 1992, p. 631. doi:10.1017/s0022112092004555.

[31] Gross, A., and Fasel, H. F., "Numerical Investigation of Supersonic Flow for Axisymmetric Cones," *Mathematics and Computers in Simulation*, Vol. 81, No. 1, 2010, pp. 133–142. doi:10.1016/j.matcom.2010.07.018.

[32] Mayer, C. S. J., "Numerical Investigation of the Nonlinear Transition Regime in Supersonic Boundary Layers," Ph.D. thesis, University of Arizona, 2009.

[33] Zhou, H., "Coherent Structure Modeling and its Role in the Computation of Passive Quantity Transport in Turbulent Flows." *JSME International Journal Series B*, Vol. 41, No. 1, 1998, pp. 137–144. doi:10.1299/jsmeb.41.137.

[34] Tam, C. K. W., and Chen, P., "Turbulent Mixing Noise from Supersonic Jets," *AIAA Journal*, Vol. 32, No. 9, 1994, pp. 1774–1780. doi:10.2514/3.12173.

[35] Tam, C. K. W., and Chen, K. C., "A Statistical Model of Turbulence in Two-dimensional Mixing Layers," *Journal of Fluid Mechanics*, Vol. 92, No. 2, 1979, pp. 303–326. doi:10.1017/S002211207900063X.

[36] Palacios, F., Economon, T. D., Aranake, A., Copeland, S. R., Lonkar, A. K., Lukaczyk, T. W., Manosalvas, D. E., Naik, K. R., Padron, S., Tracey, B., Variyar, A., and Alonso, J. J., "Stanford University Unstructured (SU2): Analysis and Design Technology for Turbulent Flows," *52nd Aerospace Sciences Meeting*, AIAA Paper No. 2014-0243, 2014. doi:10.2514/6.2014-0243.

[37] Laible, A. C., "Numerical Investigation of Boundary-Layer Transition for Cones at Mach 3.5 and 6.0," Ph.D. thesis, University of Arizona, 2011.